Cold Regions Science and Technology 219 (2024) 104108

Contents lists available at ScienceDirect

Cold Regions Science and Technology

journal homepage: www.elsevier.com/locate/coldregions

# Small-scale computational fluid dynamics modelling of the wave induced ice floe-grease ice interaction in the Antarctic marginal ice zone

Rutger Marquart [a,*], Alfred Bogaers [b], Sebastian Skatulla [a], Alberto Alberello [c], Alessandro Toffoli [d], Carina Schwarz [e]

[a] Department of Civil Engineering, University of Cape Town, Ring Road, Rondebosch, Cape Town 7700, South Africa
[b] Ex Mente Technologies, 447 Monica Rd, Lynnwood, Pretoria 0081, South Africa
[c] School of Mathematics, University of East Anglia, Norwich Research Park, Norwich NR4 7TJ, United Kingdom
[d] Department of Infrastructure Engineering, University of Melbourne, Block C, Kernot Rd, Parkville VIC, Melbourne 3010, Australia
[e] Institute of Mechanics, University of Duisberg-Essen, Universitätsstraße 2, Essen 45141, Germany

ARTICLE INFO

*Keywords:*
CFD
Sea ice rheology
Marginal ice zone
Ice floe collision
Ice floe-grease ice interaction
OpenFOAM

ABSTRACT

Computational sea ice models have been developed to simulate sea ice formation, melt and motion characteristics on a regional scale. However, the highly dynamic sea ice behaviour in the Antarctic marginal ice zone (MIZ), the area where sea ice and ocean waves interact, still eludes reliable prediction. This is due to the complex sea ice composition consisting of relatively small and mobile ice floes governed by collision and fracture mechanisms. To improve the accuracy of sea ice models, the realistic sea ice distribution needs to be accounted for at a high resolution so that key aspects defining the interplay of ice motion and wave propagation can be suitably distinguished. In this work a computational fluid dynamics model based on the small-scale continuum approach has been developed to simulate the dynamics of a heterogeneous sea ice cover. The model makes use of a realistic sea ice layout and studies the mechanical behaviour of sea ice as affected by wave forcing and the specific material properties of ice floes and grease ice. Taking advantage of the continuum approach paired with a heterogeneous sea ice cover, the floe-grease ice interaction is elucidated by discussing detailed temporal and spatial distributions of the mechanical response of sea ice. Results show that the interplay between waves and the ice floe collision behaviour is directly controlled by sea ice inertia, where the frequency and severity of ice floe collisions increase with the wave period. Furthermore, the interaction of grease ice with ice floes through form drag at the interface leads to high localised grease ice strain rate gradients and low viscosity values due its shear thinning characteristics.

## 1. Introduction

Antarctic sea ice modulates air-sea heat, gas and momentum exchange (Vichi et al., 2019) over large areas (up to 4% of the Earth's surface in winter) and, hence, it contributes notably to the global climate (Massom and Stammerjohn, 2010). The marginal ice zone (MIZ) is the exterior area where open ocean processes directly affect sea ice, resulting in a highly complex system where dynamics (Wadhams et al., 2006) and thermodynamics (Massom and Stammerjohn, 2010) profoundly influence the seasonal cycle of sea ice advance and retreat (Eayrs et al., 2019). A typical feature of the Antarctic MIZ, particularly during the winter expansion (Alberello et al., 2019), is the presence of highly mobile pancake ice floes with interstitial grease ice and areas of open water (Kohout et al., 2014; Alberello et al., 2020; Skatulla et al., 2022). The damping effect of interstitial grease ice, which exhibits a highly nonlinear viscous rheology (Paul et al., 2021), has been shown to significantly influence wave propagation and attenuation in models (Alberello and Părău, 2022), laboratory experiments (Zhao and Shen, 2015; Rabault et al., 2019) and in-situ observations (Rogers et al., 2016), in particular during the stages of sea ice advancement. The motion of ice constituents, i.e. ice floes and grease ice, relative to each other and the underlying ocean boundary layer are linked to floe ridging and welding, frazil ice scavenging and grease ice congelation (Doble, 2009; Roach et al., 2018). Large strain rates in grease ice result in turbulent motion of frazil ice crystals which will effectively prevent its consolidation (Shen et al., 1987). While wave action is believed to be the determining feature

* Corresponding author.
*E-mail address:* rutger.marquart@uct.ac.za (R. Marquart).

https://doi.org/10.1016/j.coldregions.2023.104108
Received 12 December 2022; Received in revised form 1 June 2023; Accepted 21 December 2023
Available online 28 December 2023

of pancake ice formation and dynamics (Zhao and Shen, 2015), in-situ data needed to verify the existing theoretical models are limited (Montiel et al., 2018, 2022; Kohout et al., 2020). Therefore a direct link between ice characteristics (sea ice morphology, type and thickness) and its mechanical properties (viscosity and shear modulus) is missing. In this respect, the accurate modelling of the interrelation between ice characteristics and its mechanical properties is important not only to predict sea ice dynamics and wave energy dissipation (Vichi et al., 2019; Alberello et al., 2020, 2022), but also to advance understanding of the governing mechanisms of sea ice growth in the MIZ.

Deep into the Antarctic MIZ (with up to 100% sea ice concentration), the wave-ice interaction is characterised by inelastic wave-induced deformations and fragmentation of the ice cover, wave scattering by cracks, leads or pressure ridges (Squire, 2020; Massom and Stammerjohn, 2010), inelastic floe collision (Herman, 2018), and turbulent eddy generation at the ice-water interface due to skin drag and floe-grease ice interaction (Kohout et al., 2011; Rogers et al., 2016; Smith and Thomson, 2020; Sutherland et al., 2019). The latter comprises form drag and Froude-Krylov force (Herman et al., 2019). Skin drag was also found to be significant for high relative post-collision velocities which was also confirmed by experiments (Yiew et al., 2017). The use of a two-layer model, where the stress field perturbation at the grease-ice floe interface was averaged over a single idealised floe, resulted in unrealistic ice thickness values (De Santi and Olla, 2017; De Santi et al., 2018). The three-layer model by Zhao and Shen (2018) distinguished between a turbulent boundary layer and an inviscid layer underneath which improved on the nonlinear coupling between ice and water layers. Wave steepness (the ratio of wave height to wavelength) was shown to directly impact on the restitution coefficient (Li et al., 2020). In summary, there is a strong need to accurately translate the different characteristics of sea ice, subjected to external waves and current forcing, into corresponding mechanical behaviour of sea ice via a suitable rheology.

Most of the large- and meso-scale sea ice dynamics models are continuum models and do not resolve the detailed heterogeneous sea ice composition. Finer-scale models on a floe level commonly use either a molecular dynamics schemes based on Hertzian collision dynamics (Shen et al., 1987; Hopkins, 1996; Bennetts and Williams, 2015; Rabatel et al., 2015; Herman, 2016) or the Discrete-Element method (Damsgaard et al., 2018; Herman et al., 2019). These models describe sea ice as a collection of interacting particles, therefore simplifying the solid mechanics of the individual floe and the fluid-structure interaction. Moreover, the viscous behaviour of grease ice cannot be explicitly incorporated. In contrast to discrete particle models, the continuum approach developed by Marquart et al. (2021) can account for (i) the heterogeneous ice cover composition in terms of geometrical layout of ice floes and interstitial grease ice, (ii) their respective material properties describing the solid-like deformation behaviour of ice floes and the fluid-like viscous behaviour of grease ice by their own respective material law, and (iii) the complex fluid-structure interaction between ice floes and surrounding grease ice as linked to the actual distribution floe shapes and sizes.

Here we adopt the continuum framework by Marquart et al. (2021) to study ice floe motion and collisions due to wave action, considering their realistic embedment in the surrounding grease ice. This allows for the detailed quantification of the impact of floe and grease ice material properties, geometrical features (ice floe size, shape and concentration), and wave forcing on the mechanical response of the sea ice cover. A realistic sea ice layout is extracted from in-situ image and video material recorded in the Antarctic MIZ (Alberello et al., 2022) and suitable material parameter values are chosen to independently describe the mechanics of ice floes and grease ice. We focus on the high-resolution ice rheology and exclude ice floe cohesion and ridging (seldom observed in the field), ice growth and wave attenuation by considering short time periods (less than a minute). Specifically, the stress and strain rate response of ice floe-grease ice interaction and ice floe collision dynamics is elucidated as linked to grease ice viscosity and when subjected to ocean waves. A sketch of the sea ice on top of the ocean surface in the $(x,z)$-plane is shown in Fig. 1. Note, however, that the sea ice velocity in the two-dimensional small-scale model in OpenFOAM is solved for in the basal plane, which is the $(x,y)$-plane. The origin of the Cartesian coordinate system is fixed at the mean wave elevation level ($\eta = 0$ m).

## 2. Sea ice model

The continuous two-dimensional small-scale model in the $(x,y)$-plane by Marquart et al. (2021) is briefly summarised. The momentum balance equation is:

$$m\left(\frac{\partial \boldsymbol{U}}{\partial t} + (\boldsymbol{U}\cdot\nabla)\boldsymbol{U}\right) = \boldsymbol{\tau}_a + \boldsymbol{\tau}_o + \boldsymbol{\tau}_w + \nabla\cdot\boldsymbol{\sigma}, \tag{1}$$

where $m$ and $\boldsymbol{U}$ are the sea ice mass and velocity vector respectively, $t$ is the time, $\boldsymbol{\tau}$ are the in-plane stress vectors due to external forcing contributions (wind $\boldsymbol{\tau}_a$, ocean current $\boldsymbol{\tau}_o$, and waves $\boldsymbol{\tau}_w$) and $\boldsymbol{\sigma}$ is the Cauchy stress tensor that represents the internal reaction forces. An imposed wave is considered, derived from the linear wave theory (Holthuijsen, 2007). The in-plane wave stress vector consists of two components:

$$\boldsymbol{\tau}_w = \boldsymbol{\tau}_{sd} + \boldsymbol{\tau}_{fk}, \tag{2}$$

where $\boldsymbol{\tau}_{sd}$ represents a viscous component linked to skin drag on the ice-ocean interface and $\boldsymbol{\tau}_{fk}$ the Froude-Krylov force accounting for the horizontal surge force due to the wave-induced pressure acting at the ice floe circumference (Herman, 2018). The skin drag can be written as:

$$\boldsymbol{\tau}_{sd} = \rho_w C_w |\boldsymbol{U}_w - \boldsymbol{U}|((\boldsymbol{U}_w - \boldsymbol{U})cos\theta_w + (\boldsymbol{U}_w - \boldsymbol{U}) \times \boldsymbol{k} sin\theta_w), \tag{3}$$

where $\rho_w$ and $C_w$ represent the water density and the ice-ocean drag coefficient, respectively. $\theta_w$ is the ice-ocean turning angle and $\boldsymbol{k}$ a unit vector normal to the ice surface. The wave forcing in the $(x,z)$-plane is introduced by imposing the orbital velocity of the water, $\boldsymbol{U}_w$, for a linear monochromatic wave:

$$\boldsymbol{U}_w = \begin{pmatrix} U_{w_x} \\ U_{w_y} \\ U_{w_z} \end{pmatrix} = \begin{pmatrix} a\omega sin(\omega t - kx) \\ 0 \\ a\omega cos(\omega t - kx) \end{pmatrix}, \tag{4}$$

where the Cartesian $x$-coordinate is taken along the main direction of wave propagation and $z$ in the vertical direction (the horizontal wave velocity component in the $y$-direction is zero). Parameters $a$, $\omega$ and $k$ represent the wave amplitude, wave frequency and wave number, respectively. The wave frequency and wave number, $\omega = 2\pi/T$ and $k = 2\pi/\Lambda$, are computed from the wave period $T$ and the wavelength $\Lambda$, using the deep water dispersion relation $\omega^2 = gk$. The wave orbital velocity gradient drives relative motion of floes towards/away from each

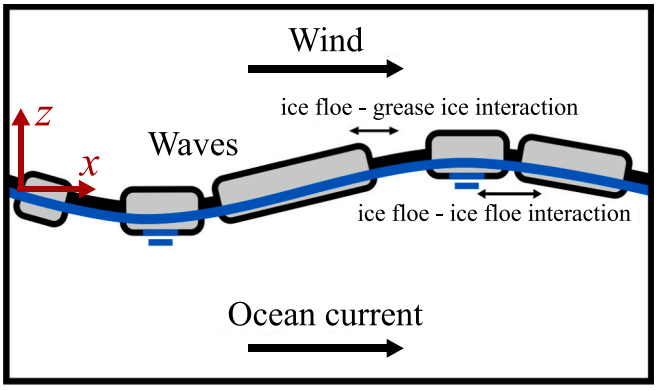


**Fig. 1.** Schematic of the ocean cover in the $(x,z)$-plane, which is subjected to a wind, ocean current and wave forcing. The ice floes and interstitial grease ice are represented by the grey rectangular shapes and a black line, respectively.

other causing floe collisions, also observed from shipboard cameras in Beaufort Sea MIZ October–November 2015 (Smith and Thomson, 2020). The Froude-Krylov force, $\boldsymbol{\tau}_{fk}$, is:

$$\boldsymbol{\tau}_{fk} = -\int_{h_w} p\boldsymbol{n}\,\mathrm{d}z, \tag{5}$$

where $h_w$ represents a portion of the submerged ice floe thickness. $\boldsymbol{n}$ indicates the unit vector, which acts normal to the ice floe circumference and is directed outwards. The wave-induced pressure, $p$, can be written as:

$$p = \rho_w g a \sin(\omega t - kx), \tag{6}$$

where $g$ indicates the gravitational acceleration. The form drag, also acting at the ice floe circumference, is implicitly included due to velocity differences between ice floes and the surrounding grease ice obeying the continuity requirement at the ice floe-grease ice interface. The latter also influences the velocity restitution of deformed colliding floes. Note that the relative motion between grease ice and ice floes is neglected due to a velocity discontinuity at the interface. As such, the form drag is not fully accounted for.

In summary, the sea ice velocity is only solved in the $x$- and $y$-direction, whereas the orbital wave velocity is defined in the three-dimensional space. As a result, the skin drag, $\boldsymbol{\tau}_{sd}$, has a component in the $z$-direction. Consequently, the wave stress vector, $\boldsymbol{\tau}_w$, contains three components, but only its in-plane components enter the momentum balance equation.

Two ice materials are considered in the small-scale model, namely ice floes and grease ice, each with its own material law. Ice floes are modelled as a solid-like material via generalised Hooke's law in three dimensions:

$$\boldsymbol{\sigma}_{floe} = 2\mu\boldsymbol{\varepsilon} + \lambda\boldsymbol{I}\,\mathrm{tr}(\boldsymbol{\varepsilon}), \tag{7}$$

where $\mu$ and $\lambda$ represent the Lamé constants, $\boldsymbol{\varepsilon}$ the strain tensor and $\boldsymbol{I}$ the identity tensor. Grease ice, on the other hand, behaves as a viscous fluid which is described by a viscous-plastic material law similar to e.g. Hibler (1979a) and Thorndike et al. (1975). The grease ice material law is:

$$\boldsymbol{\sigma}_{grease} = 2\eta\dot{\boldsymbol{\varepsilon}} + \boldsymbol{I}\left((\zeta-\eta)\mathrm{tr}(\dot{\boldsymbol{\varepsilon}}) - \frac{P}{2}\right), \tag{8}$$

where the strain rate tensor is denoted by $\dot{\boldsymbol{\varepsilon}} = \frac{1}{2}\left(\nabla\boldsymbol{U} + (\nabla\boldsymbol{U})^T\right)$ and the grease ice strength parameter by $P$. The coupled strain rate-dependent bulk and shear viscosities, denoted by $\zeta$ and $\eta$, respectively, are:

$$\zeta = \frac{P}{2\Delta} \quad \text{and} \quad \eta = \frac{\zeta}{e^2}, \tag{9}$$

where the effective strain rate parameter, $\Delta$, is defined as:

$$\Delta = \sqrt{\left(\dot{\varepsilon}_{11}^2 + \dot{\varepsilon}_{22}^2\right)(1+e^{-2}) + 4e^{-2}\dot{\varepsilon}_{12}^2 + 2\dot{\varepsilon}_{11}\dot{\varepsilon}_{22}(1-e^{-2})}. \tag{10}$$

The latter has a lower limit, $\Delta = 2{\cdot}10^{-7}\,\mathrm{s}^{-1}$ (Leppäranta and Hibler (1985)), to ensure that viscosity values do not become infinite when the strain rates tend to zero. Parameter $e$ represents the eccentricity, which is the ratio between the in-plane principal axes of the elliptical yield curve used by Hibler (1979b). The in-plane Cartesian components of the symmetric strain rate tensor are $\dot{\varepsilon}_{11}$, $\dot{\varepsilon}_{22}$ and $\dot{\varepsilon}_{12}$.

The small-scale model has been implemented in the open source computational fluid dynamics software OpenFOAM. The sea ice domain is represented by a Finite Volume Method (FVM) and both ice constituents are spatially distinguished by means of the volume of fluid method (VoF) that numerically describes the interface between immiscible and incompressible fluids (Roenby et al., 2016, 2019). The assumptions of this approach are: (i) only short time periods, less than a minute, are considered during which the temperature can be assumed constant, and therefore thermodynamic ice growth/melt is negligible; (ii) failure or fracture of ice floes is disregarded; and (iii) cohesion and ridging phenomena are excluded.

The numerical investigation focuses on the interaction between ice floes and grease ice within a realistic sea ice domain subjected to a harmonic propagating gravity wave.

For modelling purposes, the $100 \times 100\,\mathrm{m}^2$ problem domain depicted in Fig. 2 (left) is embedded in a $300 \times 300\,\mathrm{m}^2$ outer domain to which zero-gradient boundary conditions (BCs) are applied at the edges. The gradient of all variables in the direction perpendicular to the boundary is assumed zero, resulting in a minor error at the boundaries. Consequently, the boundary was chosen to be sufficiently far from the region of interest, so that it only affects cells neighbouring the BC and not the inner domain. Hence, the BC as applied, by modelling a much larger area, acts as a dampening boundary. The entire domain is discretised by a uniform grid of $0.33 \times 0.33\,\mathrm{m}^2$ FVM cells for all simulations. The floe size distribution is extracted from in-situ imaging of the Antarctic MIZ (Alberello et al., 2019).

A high-resolution analysis of the sea ice dynamics and its characterising rheology variables will be performed. The ice floe and grease ice properties, and wave characteristics are summarised in Table 1. Note that all terms used in the small-scale model are normalised by their respective density (ice floe and grease ice). The ice floe and grease ice thickness values have been obtained from Skatulla et al. (2022) and Worby et al. (2008), and the density values from McGuinness et al. (2009), Radia (2014), Schulkes et al. (1998) and Skatulla et al. (2022). The effective elastic ice floe parameters are based on values for uncompacted snow (Shapiro et al., 1997), assuming that the very soft edges of pancake ice floes (Doble et al., 2003) dominate the floe deformation behaviour for gentle collisions. The three kinematic grease ice viscosity values agree with literature values (Wadhams et al., 2006; Newyear and Martin, 1999; Wang and Shen, 2010; Paul et al., 2021). The grease ice yield surface parameter is from Hibler (1979b), Hunke and Dukowicz (1997) and Leppäranta and Hibler (1985). The grease ice strength parameters are determined such that the resulting domain-averaged viscosity values, which are affected by strain rate capping, correspond to the kinematic grease ice viscosity values.

Our focus is on the mechanics of wave-ice interaction, therefore the effects of ocean and wind currents, $\boldsymbol{\tau}_o$ and $\boldsymbol{\tau}_a$, are excluded (they are homogeneous at the small scale considered here, and only become relevant at larger scales where gradients in their field exist). The external forcing results only from the wave action via the Froude-Krylov force acting on submerged part of floe edge, $h_w$, and the skin drag on the entire ice-ocean interface. The latter is controlled by the drag coefficient, $C_w$ (Lu et al., 2011; Andreas et al., 1984; McGuinness et al., 2009). The forcing wave characteristics are defined by five wave periods and a prescribed wave steepness, $ak = 0.06$, which is chosen to match stormy wave conditions in the Southern Ocean (Derkani et al., 2021). All

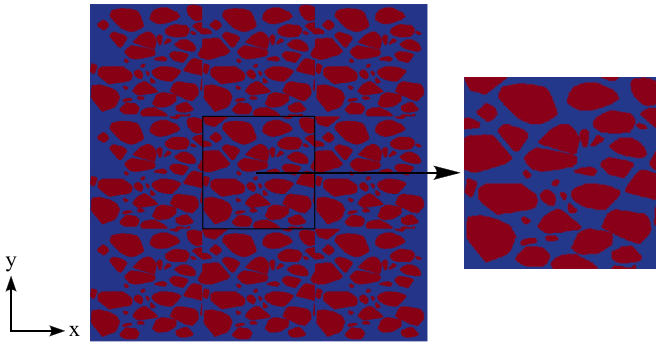


**Fig. 2.** Realistic sea ice layout showing a $100 \times 100\,\mathrm{m}^2$ inner domain with $9{\times}10^4$ FVM cells (right), embedded in a $300 \times 300\,\mathrm{m}^2$ outer domain with $81{\times}10^4$ FVM cells (left).

**Table 1**
Parameters used in the sea ice dynamics analysis. XCD (YCD) denote the caliper diameter and XSD (YSD) the standard deviation in $x$- ($y$-) direction.

| Parameter | Definition | Value | Unit |
|---|---|---|---|
| $D_{x,y,median}$ | median ice floe XCD, YCD | 13, 10 | m |
| $SD_{x,y}$ | XSD, YSD | 8.8, 5.5 | m |
| $h_{i,g}$ | thickness ice floes, grease ice | 0.31, 0.1 | M |
| $\rho_{i,g}$ | density ice floes, grease ice | 879, 997 | Kg m$^{-3}$ |
| $A$ | ice floe area fraction | 54.7 | % |
| $\lambda_i$ | first Lamé parameter ice floes | $6.4 \times 10^6$ | Nm$^{-2}$ |
| $\mu_i$ | second Lamé parameter ice floes | $3.3 \times 10^6$ | Nm$^{-2}$ |
| $\nu$ | kinematic grease ice viscosity | 0.01, 0.04, 0.16 | m$^2$ s$^{-1}$ |
| $P^*$ | grease ice strength parameter | 0.006, 0.024, 0.096 | Nm$^{-2}$ |
| $e$ | eccentricity grease ice | 2 | – |
| $C_{w,i}$ | ice-ocean drag coefficient ice floes | 0.02 | – |
| $C_{w,g}$ | ice-ocean drag coefficient grease ice | 0.008 | – |
| $\theta_w$ | ice-ocean turning angle | 0 | ° |
| $T$ | wave period | 12, 14, 16, 18, 20 | S |
| $a$ | wave amplitude | 2.1, 2.9, 3.8, 4.8, 6 | m |
| $\Lambda$ | wavelength | 225, 306, 400, 506, 625 | m |

simulations are run for $t = 60$ s and at a time resolution of $t = 0.01$ s. Only the last 30 s are analysed, when the velocity of sea ice reaches near steady-state conditions. The initial conditions of the variables related to both the ice floe and grease ice rheologies; stress, $\boldsymbol{\sigma}$, strain rate, $\dot{\boldsymbol{\epsilon}}$, bulk and shear viscosity, $\zeta$ and $\eta$, and velocity, $\boldsymbol{U}$, are set to zero.

## 3. Sea ice dynamics

### 3.1. Ice floe motion and collisions

The orbital wave velocity in $x$-direction of an imposed gravity wave with $T = 12$ s, propagating along the $x$-direction through the 100 × 100 m$^2$ inner domain, is shown in Fig. 3(a-e), for times spanning one wave period (from $t = 38$ s to $t = 50$ s).

The sea ice velocity in $x$-direction, depicted in Fig. 3(f–j) for a grease ice viscosity of $\nu \approx 0.04$ m$^2$ s$^{-1}$, results from the orbital velocity gradient. The sea ice velocity is characterised by a delayed response and clear floe size-dependent differences, both due to the effect of inertia. Additionally, a few ice floes in the wave trough and wave crest clearly show a velocity gradient within the ice floes, due to the wave displacement. Temporary contact between ice floes occurs when neighbouring floes share the same velocity magnitude. The oscillatory nature of the orbital wave velocity yields a mostly periodic back and forth motion of the floes with negligible net-resultant horizontal movement of ice floes over time (drift). At $t = 38$ s, ice floes at the centre of the domain are located in an ascending wave flank with zero orbital wave velocity in the $x$-direction and maximum positive floe velocity indicating a sliding of ice floes in the forward direction. At $t = 41$ s, the centrally located ice floes are in the wave trough and have the largest negative orbital wave velocity. Due to inertia, the floe velocity in the $x$-direction is close to zero, therefore indicating a phase shift between orbital wave velocity and sea ice velocity. At $t = 44$ s, the floes at the centre have maximum negative velocity in $x$, the ice floe motion is diverging in the wave trough. At $t = 47$ s and $t = 50$ s, floe motion at the wave crest is converging.

The effects of the velocity phase shift can be observed in Fig. 4 which presents the temporal evolution of the domain-averaged ice floe normal stress tensor component, $\sigma_{xx}$, and the velocity vector component, $U_x$. Two wave periods are shown, $T = 12$ s and $T = 20$ s. The extrema, representing both the curve maximum and minimum of ice floe stress, coincide with the extrema of ice velocity and the gradient of orbital wave velocity, where the Froude-Krylov force is maximum. The effect of gravity-induced sliding of ice floes downwards on both wave flanks would lead to the opposite motion behaviour, but can be considered negligible (Herman, 2018).

The Froude-Krylov force acting at the submerged circumference of

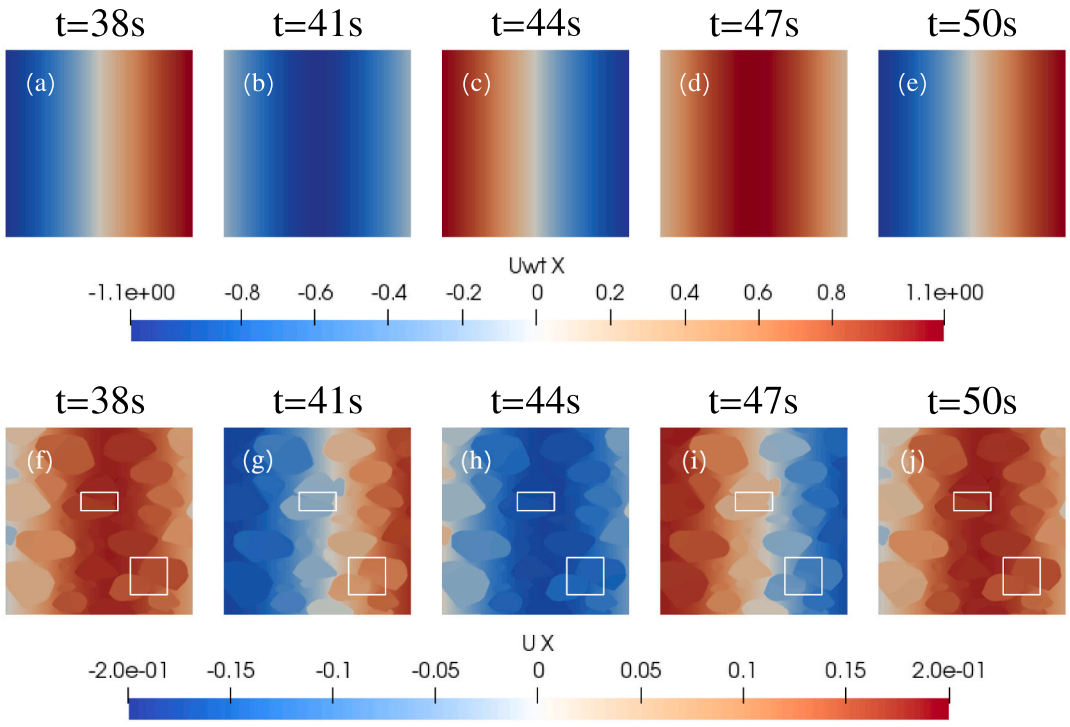


**Fig. 3.** (a–e) Imposed wave velocity, $U_{w_x}(\mathbf{x}, t)$ [m s$^{-1}$], and **(f–j)** resulting sea ice velocity, $U_x(\mathbf{x}, t)$ [m s$^{-1}$], along the $x$-direction for $T = 12$ s and kinematic grease ice viscosity $\nu \approx 0.04$ m$^2$ s$^{-1}$ at various times. The white rectangles at the bottom-right and in the centre mark locations of floe collisions, referred to as Zone I and Zone II, respectively.

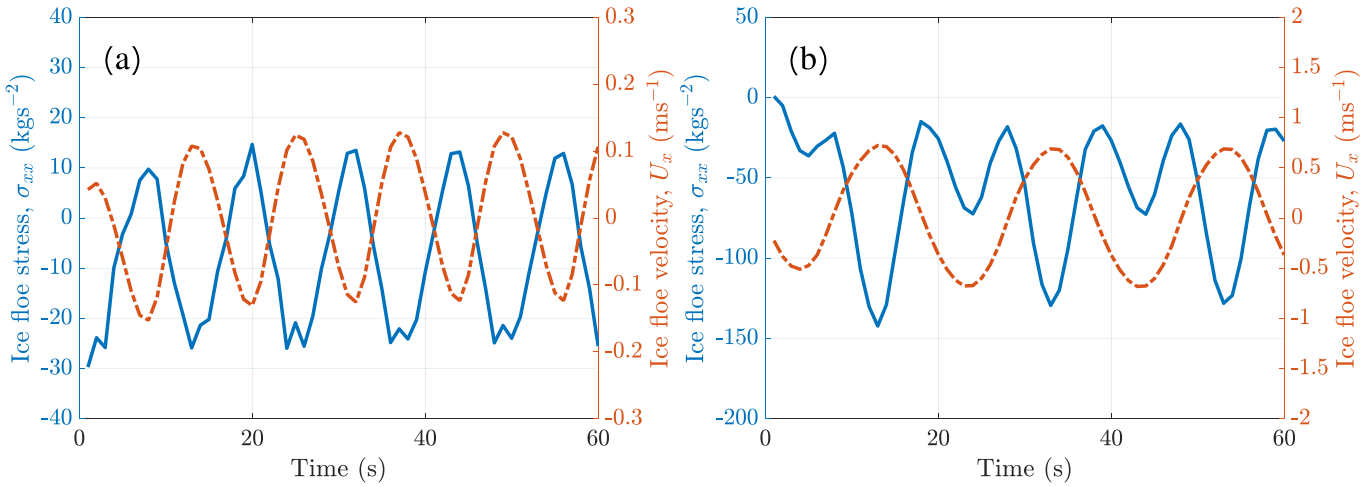


**Fig. 4.** Domain-averaged sea ice response due to imposed wave forcing for kinematic grease ice viscosity $\nu \approx 0.04\ \mathrm{m^2\,s^{-1}}$ illustrating the first component of the ice floe stress tensor component, $\sigma_{f,xx}$, and the ice floe velocity in $x$-direction, $U_x(\mathbf{x}, t)$ for waves with **(a)** $T = 12$ s, and **(b)** $T = 20$ s.

the ice floes depends on the wave displacement, and, hence, the velocity gradient. The latter can be clearly observed in the velocity vector fields in Fig. 5(a-e), where the velocity vectors change in colour within several floes. This results in a stress magnitude gradient in the ice floes, as shown in Fig. 5(f-j). Additionally, the areas marked by white rectangles highlight the evolution of two ice floe collisions for a wave forcing with $T = 12$ s which are characterised as points of highly localised stress magnitudes. The floe interaction is not characterised by short violent collisions but rather continuous churning contact varying in intensity.

Colliding ice floes temporarily show shared velocity values and directions at contact, as seen in Fig. 3(f–j) and Fig. 5(f–j). For the ice floe collision in the bottom-right (Zone I), the collision stress is most intense when the two colliding floes leave the trough, at $t = 41$ s (Fig. 5(b)), and when entering the crest $t = 47$ s (Fig. 5(d)). Similarly, the floe collision found at the centre of the domain (Zone II) exhibits a high stress intensity when the two floes are at the crest, at $t = 38$ s and at $t = 50$ s, and leave the trough, at $t = 44$ s.

The velocity vector contour plots in Fig. 5(f–j) for $T = 12$ s highlight the velocity differences of ice floes and the surrounding grease ice, where only the former are affected by form drag and collision-induced rotation. Vertical bands along which, due to the orbital sea ice motion, the velocity vectors point in opposite direction on either side indicate floes being located between trough and crest.

The minimum principal stress, $\sigma_{min}$, which if negative indicates

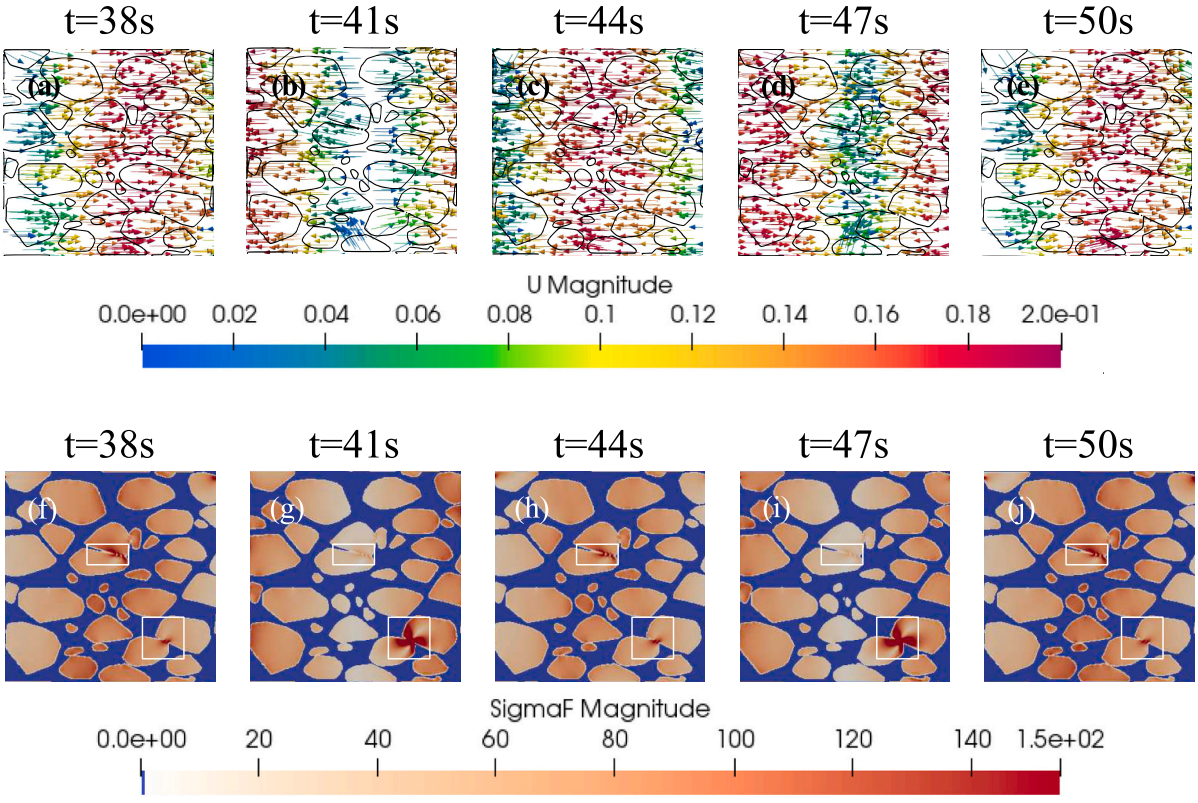


**Fig. 5.** (a–e) Velocity vector field $\mathbf{U}(\mathbf{x}, t)$ [m s$^{-1}$]. and **(f–j)** ice floe stress magnitude field, $\sigma_{f,mag}(\mathbf{x}, t)$ [kg s$^{-2}$], with ice floe collisions at points of high localised stress, for $T = 12$ s and kinematic grease ice viscosity $\nu \approx 0.04\ \mathrm{m^2\,s^{-1}}$.

maximum compressive stress acting normal to the plane where shear stress is zero, provides an indication of the collision stress intensity. Contour plots of the minimum principal ice floe stress for wave forcings $T = 12$ s and $T = 20$ s, illustrated in Fig. 6, show the evolution of ice floe collisions over time. Note that the legends differ, as stresses are wave period dependent. The longer wave ($T = 20$ s) yields a higher number of ice floe collisions, whereas for shorter waves ($T = 12$ s) only a few pairs of floes interact with each other, specifically, floes which have been in close vicinity at $t = 0$ s (for example as marked by the white rectangles in Zones I and II). Differences in ice floe collision patterns are due to an increasing wave kinetic energy for longer wave period for a fixed value of steepness.

The relation between wave elevation, velocity and ice floe collision stress intensity over time are discussed for the ice floe collisions occurring in Zone I and Zone II for waves of period $T = 12$ s, $T = 16$ s and $T = 20$ s. The minimum principal stress collision intensity over a time window of one wave period yields a peak stress collision intensity equal to $\sigma_{col}^{peak} = -973\,\mathrm{kg\,s^{-2}}$, $-1186\,\mathrm{kg\,s^{-2}}$, and $-1535\,\mathrm{kg\,s^{-2}}$ in Zone I for the three different periods, i.e. the absolute value increase with wave period. In Zone II, the absolute magnitudes are reduced but the the trend is similar to Zone I. In this case the minimum principal stress are $\sigma_{col}^{peak} = -371\,\mathrm{kg\,s^{-2}}$, $-410\,\mathrm{kg\,s^{-2}}$, and $-541\,\mathrm{kg\,s^{-2}}$, respectively.

Ice floe collisions occur for all five wave periods analysed, but their number increases with the wave period, as found by visual inspection of Fig. 6(a-e) as opposed to Fig. 6(f–j). This is also reflected by the percentages of FVM cells exhibiting highly localised minimum principal stress values, i.e. $> 2$ MPa (Shapiro et al., 1997; Skatulla et al., 2022), which is only 0.10%, 0.50% and 1.18% for wave periods $T = 12$ s, $T = 16$ s and $T = 20$ s, respectively. The same ice floes tend to collide multiple times for wave periods with $T < 16$ s, whereas various ice floes collide for the larger wave periods ($T \geq 16$ s). In the latter case, the multiple floes collisions are attributed to a higher kinetic wave energy and more intense inertia effects linked to the oscillatory floe motion.

In Fig. 7(a) box plots show the minimum principal stress values of all ice floe FVM cells in the inner domain over one wave period with $\nu \approx 0.04\,\mathrm{m^2\,s^{-1}}$ and for the five wave periods (from $T = 12$ s to $T = 20$ s). For all wave periods data are skewed. All FVM cell-values in the inner domain beyond the maximum and minimum whisker length are defined as statistical outliers(indicated by red plus symbols in Fig. 7). Specifically, the negative minimum principal stress outliers refer to ice floe portions under severe compression as found in floe collision zones illustrated in Fig. 6. The corresponding lower adjacent in the box plot, shown in Fig. 7(a), is used to define the collision stress threshold, and equals $\sigma_{col}^{thres} = -143\,\mathrm{kg\,s^{-2}}$, $-150\,\mathrm{kg\,s^{-2}}$, $-154\,\mathrm{kg\,s^{-2}}$, $-166\,\mathrm{kg\,s^{-2}}$, $-201\,\mathrm{kg\,s^{-2}}$ for increasing wave periods (from $T = 12$ s to $T = 20$ s), i.e. its absolute value increases. The number of extreme minimum principal stress outliers, referred to as *collision stress* in the following, indicate the number of FVM cells directly affected by floe collisions, and their number increases with the frequency and severity of floe collisions. Fig. 7(b) shows the total number of minimum principal stress outliers during one wave period in the inner domain and Fig. 7(c) shows the temporally- and domain-averaged collision stress value for all five wave forcings with kinematic grease ice viscosities $\nu \approx 0.01\,\mathrm{m^2\,s^{-1}}$, $\nu \approx 0.04\,\mathrm{m^2\,s^{-1}}$, and $\nu \approx 0.16\,\mathrm{m^2\,s^{-1}}$, respectively. The number of FVM cells associated with collisions show a clear gradual growth for increasing wave period. Consequently, the temporally- and spatially-averaged collision stress also growing for longer wave period. The stress response is not significantly impacted by changes in viscosity within the given range as found in-situ (Newyear and Martin, 1999; Paul et al., 2021; Wadhams et al., 2006; Wang and Shen, 2010). Additionally, the small-scale model enforces the wave properties, i.e. no wave attenuation is considered, that would reduce the strain rate along the wave propagation if accounted for. This effect, however, is negligible over a spatial domain comparable to the wavelength.

To study the most intense ice floe collision, i.e. those in Zone I, the mean wave elevation and collision stress intensity of both floes combined are plotted over time in Fig. 8 for wave periods $T = 12$s, $T = 16$s and $T = 20$s, respectively.

All wave periods show a similar correlation between the minimum intensity of the collision stress and the maximum compression stress just

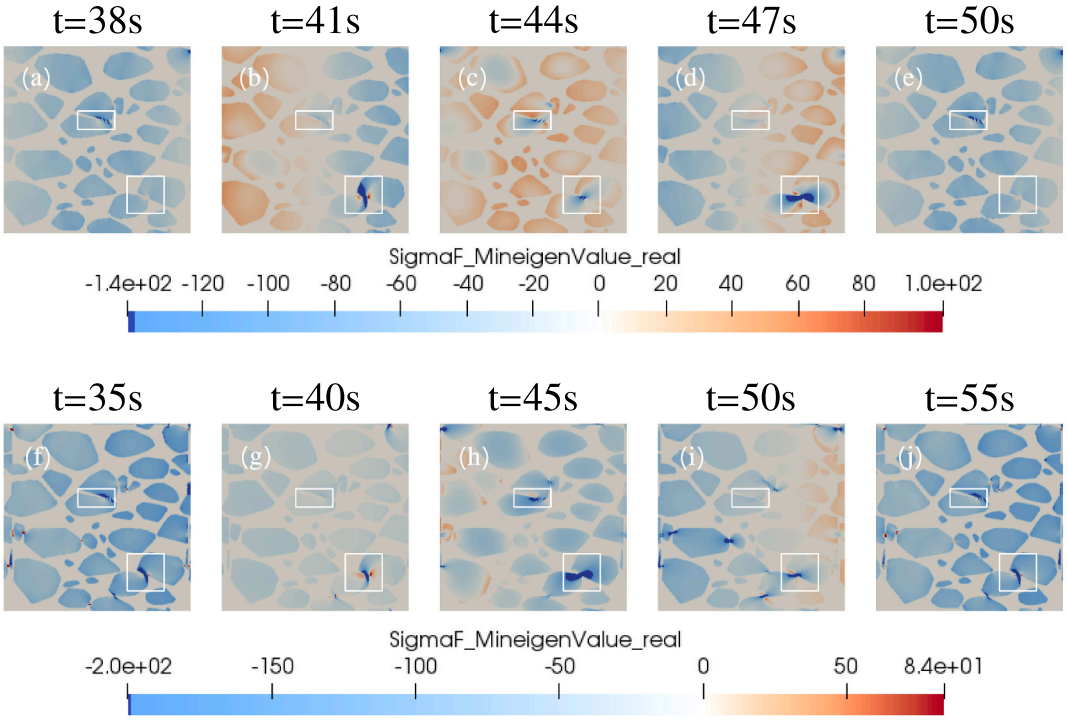


**Fig. 6.** Minimum principal stress field, $\sigma_{min}(\mathbf{x}, t)$ [kg s$^{-2}$] illustrates one wavelength with ice floe collisions at points of high stress for two different wave forcings: **(a–e)** $T = 12$ s and $\nu \approx 0.04\,\mathrm{m^2\,s^{-1}}$, and **(f–j)** $T = 20$ s and $\nu \approx 0.04\,\mathrm{m^2\,s^{-1}}$ over one wave period.

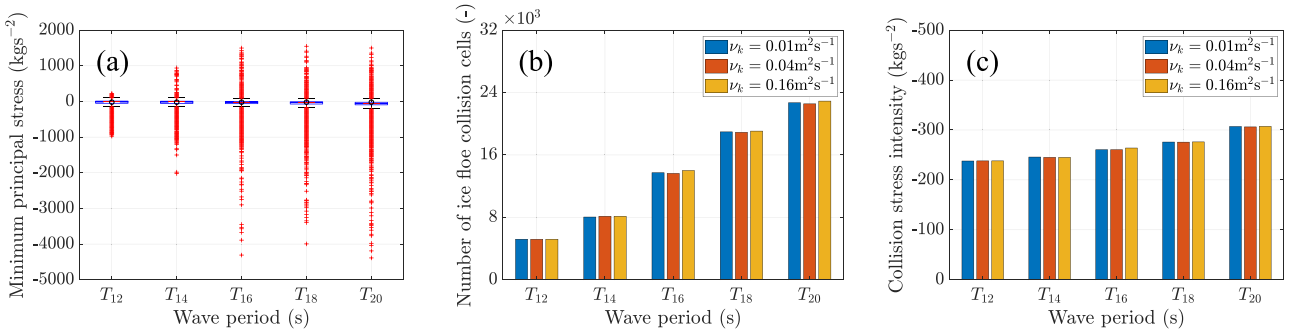


**Fig. 7.** **(a)** Box plots of the minimum principal stress [kg s$^{-2}$] of all ice floe FVM cells in the inner domain for $\nu \approx 0.04\ \text{m}^2\,\text{s}^{-1}$ and the wave periods $T = 12 - 20$ s, **(b)** number of minimum principal ice floe stress outliers (collision stress) for kinematic grease ice viscosity values ranging from $\nu \approx 0.01 - 0.16\ \text{m}^2\,\text{s}^{-1}$, and **(c)** temporally- and spatially-averaged collision stress intensityaccumulated over one wavelength for $\nu \approx 0.01 - 0.16\ \text{m}^2\,\text{s}^{-1}$.

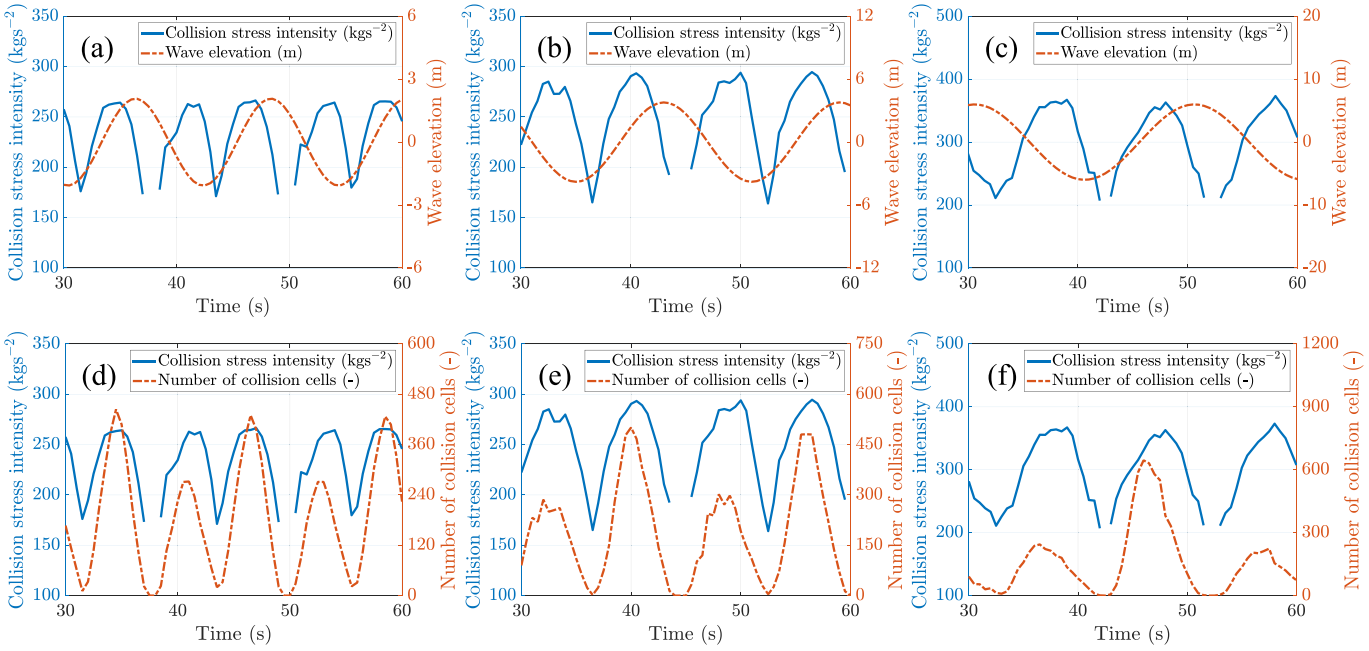


**Fig. 8.** Spatially-averaged wave elevation,collision stress intensity,and the number of ice floe collision FVM cells over time for the ice floe collision taking place in Zone I, for three different wave forcings with $\nu \approx 0.04\ \text{m}^2\,\text{s}^{-1}$: **(a,d)** $T = 12$ s, **(b,e)** $T = 16$ s, and **(c,f)** $T = 20$ s.

before and after the wave crest and wave trough, as depicted in Fig. 8 (a–c). The time-averaged collision stress intensity in Zone I over one wave period increases for longer waves, namely $\sigma_{col}^{avg} = -233\ \text{kg}\,\text{s}^{-2}$ for $T = 12$ s, $-248\,\text{kg}\,\text{s}^{-2}$ for $T = 16$ s, and $-303\ \text{kg}\,\text{s}^{-2}$ for $T = 20$ s. In Zone II the time-averaged collision stress intensity values over one wave period are less violent, i.e. $\sigma_{col}^{avg} = -184\ \text{kg}\,\text{s}^{-2}$ and $-190\ \text{kg}\,\text{s}^{-2}$, and $-250\ \text{kg}\,\text{s}^{-2}$ for a wave period with $T = 12$ s, $T = 16$ s and $T = 20$ s, respectively. The difference in collision stress is attributed to the different relative positioning of the floes. In Zone I the colliding floes are along the main direction of wave propagation whereas in Zone II they are parallel to the main wave propagation, therefore limiting the momentum transfer.

The collision stress intensity and the number FVM cells in which collision occur show a direct relation, i.e. an increase in the collision stress intensity results in an increasing number of ice floe collisions, see Fig. 8(d-f). The cumulative ice floe collisions in Zone I over one wave period are 4168, 5991 and 7608 for wave periods $T = 12$ s, $T = 16$ s and $T = 20$ s, respectively. Discontinuities in the curves of the domain-averaged collision stress intensity, see Fig. 8, indicate that the minimum principal stress of the two floes is below the previously defined collision stress threshold. This is either due to ice floes that have temporarily detached themselves leading to the absence of ice floe collision cells or due to ice floe contact with low stress intensity. In Zone II the cumulative number of collisions is 545, 843 and 1206, for wave periods $T = 12$ s, $T = 16$ s and $T = 20$ s, respectively. The same trend is, again, found for the ice floe collisions in Zones I and II, but the number of collision cells is almost one order of magnitude lower than in Zone I for the same wave period.

The local sea ice velocity and the orbital wave velocity in the $x$-direction are shown in Fig. 9 for two different wave periods, $T = 12$ s and $T = 20$ s. Ice floe collisions in the inner domain would not occur when the sea ice cover is at rest. However, due to the influence of sea ice inertia, the collision stress intensity is out of phase with the velocity and wave elevation. As a result, the relation between sea ice velocity, wave elevation and collision stress intensity is not straight-forward. The relative motion of the ice layer with respect to the ocean layer underneath is generally influenced by the wave forcing and the ice composition (Smith and Thomson, 2020). In particular, inertia of the ice cover opposing the oscillatory orbital wave velocity and the frictional contact at the ice basal plane, result in a lag of the sea ice velocity behind the orbital wave velocity. The phase shift between the sea ice velocity and

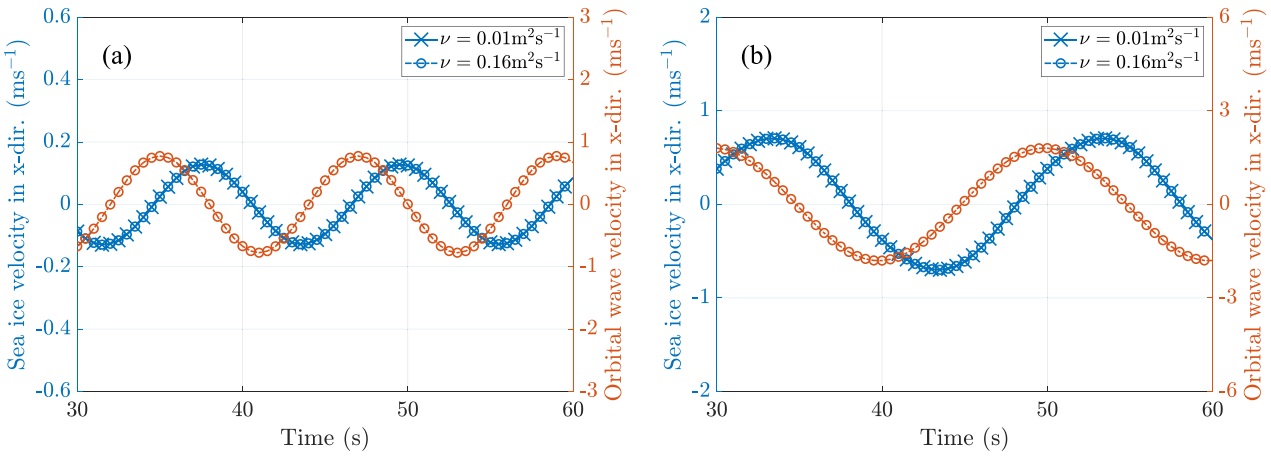


**Fig. 9.** The influence of grease ice viscosity values, $\nu \approx 0.01\ \text{m}^2\,\text{s}^{-1}$ and $\nu \approx 0.16\ \text{m}^2\,\text{s}^{-1}$, on the velocity phase shift in Zone I, for a wave period of **(a)** $T = 12\,\text{s}$, and **(b)** $T = 20\,\text{s}$.

the orbital wave velocity in the $x$-direction is constant over time and equal to 2.5 s, 3.0 s and 3.5 s, for wave periods $T = 12\,\text{s}$, $T = 16\,\text{s}$ and $T = 20\,\text{s}$, respectively. Thus, the phase shift is not the same for all wave periods, but is inversely proportional to the phase shift over the wave period, from approximately 21% to 18%. The effect of grease ice viscosity on the phase shift in Zone I is negligible considering the lowest and highest kinematic grease ice viscosity values, $\nu \approx 0.01\ \text{m}^2\,\text{s}^{-1}$ and $\nu \approx 0.16\ \text{m}^2\,\text{s}^{-1}$, see Fig. 9.

### 3.2. Ice floes and grease ice interactions

This section focuses on the interaction between ice floes and grease ice in terms of the stress, strain rate and viscosity distributions in the sea ice domain. The previously observed complex ice motions are caused by the heterogeneous sea ice composition and distinct differences in material behaviour of its two constituents (ice floes and grease ice). The viscous stress response of grease is non-linear, highly strain rate-dependent and several orders of magnitude smaller than the ice floe stress. The magnitudes of the sea ice velocity gradient and strain rate distributions are shown in Fig. 10. The strain rate magnitude distribution is qualitatively similar to the one of the velocity gradient. Note that the legends of both variables are capped to improve clarity of the contour plots. The inner domain contains values up to $\dot{\varepsilon}_{mag} \approx 0.15\ \text{s}^{-1}$ and $\nabla U_{mag} \approx 0.15\ \text{s}^{-1}$ at the interface between ice floes and grease ice. The sea ice velocity gradient, and therefore the strain rate, approaches zero when the sea ice velocity is either at its maximum or minimum. Due to the influence of inertia this corresponds to a wave elevation close to zero, in between the wave crest and the wave trough.

The grease ice bulk viscosity, $\zeta$, is a nonlinear function of the strain rate. The viscosity distribution, shown in Fig. 11(a-e), and the strain rate

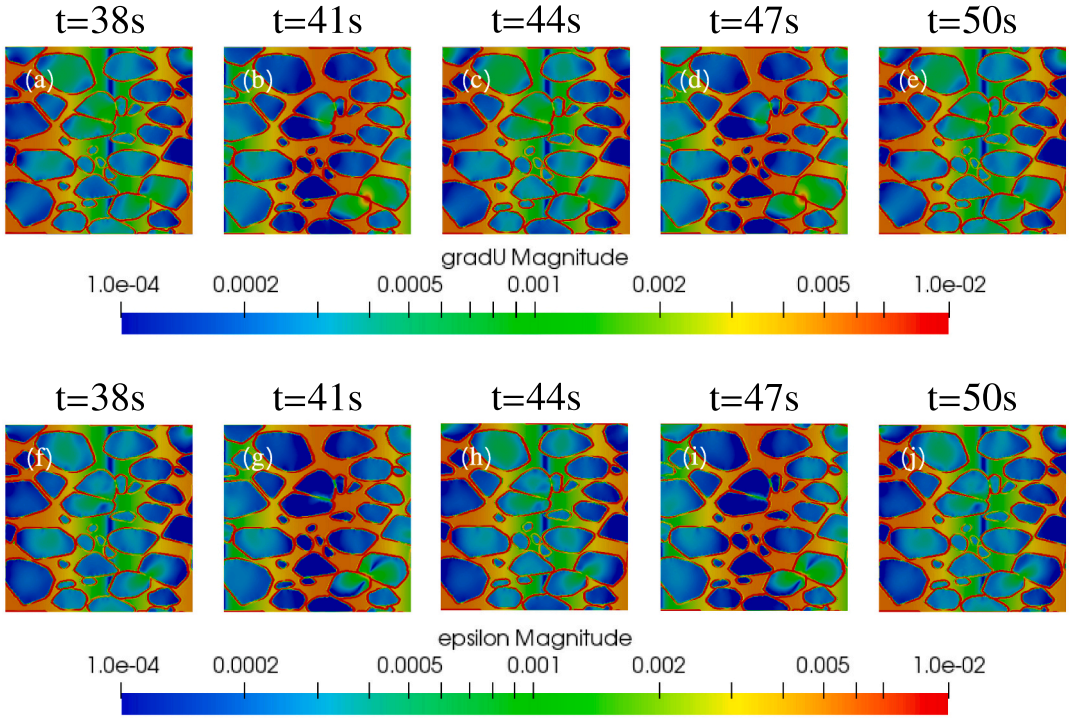


**Fig. 10.** (a–e) Velocity gradient, $\nabla U_{mag}(\mathbf{x}, t)\ \left[\text{s}^{-1}\right]$, and **(f–j)** strain rate, $\dot{\varepsilon}_{mag}\ \left[\text{s}^{-1}\right]$ for a wave $T = 12\,\text{s}$ and kinematic grease ice viscosity $\nu \approx 0.04\ \text{m}^2\,\text{s}^{-1}$ at different times.

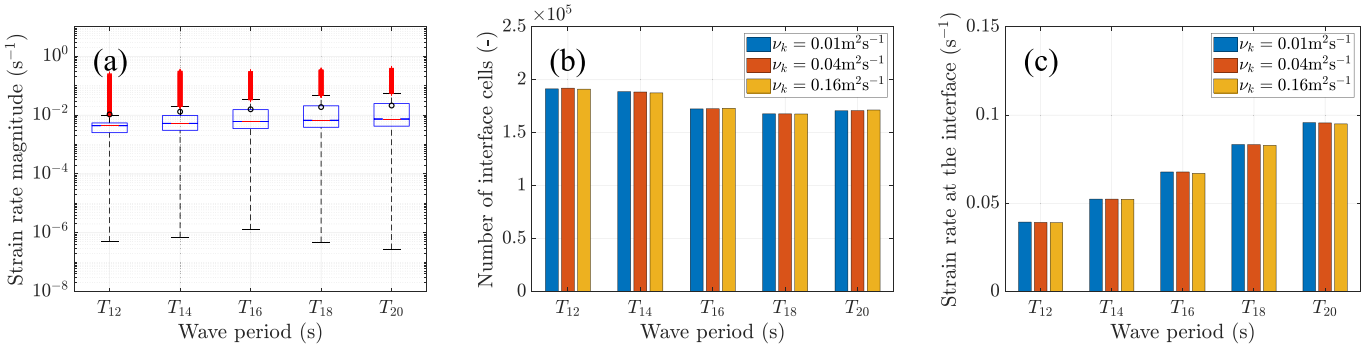


**Fig. 11.** (a–e) Bulk viscosity field, $\zeta$ [kg s$^{-1}$], **(f–j)** grease ice stress magnitude distribution, $\sigma_{g,mag}$ [kg s$^{-2}$], and **(k–o)** the spherical part of the grease ice stress tensor, $\text{sph}(\boldsymbol{\sigma}_g)$, plotted over a horizontal line, represented by white arrows for all five time steps for wave period $T = 12$ s and kinematic grease ice viscosity $\nu \approx 0.04$ m$^2$ s$^{-1}$ at various times.

suffer from a singularity with locally very high viscosity values when strain rates approach zero. Note, however, that the inner domain locally contains bulk viscosity values of $\zeta \approx 100$ kg s$^{-1}$, which are capped in the legend at $\zeta = 2$ kg s$^{-1}$, to enhance clarity in the contour plots. As expected for shear thinning behaviour, the bulk viscosity exhibits clear minima where the strain rate has maxima, in particular at the floe-grease ice interfaces.

The grease ice stress distribution, shown in Fig. 11(f–j), is due to its dependency on the strain rate a function of the velocity gradient. A sharp interface, shown in Fig. 11(f,h and j), corresponds to the position in the domain where the velocity gradient and strain rate magnitudes approach zero, leading to locally very high viscosity values. The grease ice stress magnitude distribution, including sharp interface, is studied in detail by plotting the spherical part of the grease ice stress tensor given by its trace, $\text{sph}(\boldsymbol{\sigma}_g) = \frac{1}{3}\text{tr}(\boldsymbol{\sigma}_g)$, in kg s$^{-2}$ in Fig. 11(k-o), over a horizontal line, as illustrated by white arrows in Fig. 11(f–j).

The spherical part of the grease ice stress tensor refers to stress linked to volume change (tension or compression). The graphs are directly placed under the distributions and equal in size, allowing direct comparison between the grease ice stress magnitude distributions and the evolution of $\text{sph}(\boldsymbol{\sigma}_g)$ over the horizontal line. Note that the white arrows also cross ice floes, resulting in $\text{sph}(\boldsymbol{\sigma}_g)$ values equal to zero, shown by discontinuities in the stress curves in Fig. 11(k-o). As expected for fluid-like behaviour, defined by the VP rheology in Eq. (8), $\text{sph}(\boldsymbol{\sigma}_g) \leq 0$ is found, indicating resistance capacity only in compression and shear. The diverging velocity distribution at the wave trough at $t = 41$ s (Fig. 3(g)) therefore leads to very small spherical stress values whereas the converging velocity distribution at the crest at $t = 47$ s (Fig. 3(i)) results in large spherical stress values indicating compression. At the interface, high strain rate values dominate the stress response, resulting in intermediate grease ice stress magnitude values, indicated in green.

The effect of grease ice viscosity on strain rate distributions is investigated by examining the differences in mechanical response over all five wave periods, averaged over a wave period, as depicted in Fig. 12 (a). These box plots provide information regarding interface effects between ice floes and grease ice. Each box plot represents strain rate magnitude values of all grease ice FVM cells in the inner domain with $\nu \approx 0.04$ m$^2$ s$^{-1}$ for the five wave forcings within the range of $T = 12 - 20$ s. All wave periods show sample skewness, with mean values, indicated by a black circle, ranging between $\dot{\varepsilon}_{mag} = 0.0105 - 0.0212$ s$^{-1}$. The median, indicated by a red horizontal line, ranges between $\dot{\varepsilon}_{mag} = 0.0044$ s$^{-1}$ and $\dot{\varepsilon}_{mag} = 0.0074$ s$^{-1}$. The maximum whisker lengths of $\dot{\varepsilon}_{mag} = 0.0098$ s$^{-1}$, $\dot{\varepsilon}_{mag} = 0.0196$ s$^{-1}$, $\dot{\varepsilon}_{mag} = 0.0332$ s$^{-1}$, $\dot{\varepsilon}_{mag} = 0.0460$ s$^{-1}$, $\dot{\varepsilon}_{mag} = 0.0555$ s$^{-1}$ for increasing wave period, represent the upper adjacent that serves as the threshold between the 75th percentile and the outliers.

Each outlier illustrates a FVM cell in the inner domain with an extreme strain rate value, which is located at the ice floe-grease ice interface. The number of extreme strain rate values indicate the number of interface FVM cells and how strong form drag on the ice floe-grease ice interface is. Fig. 12(b) shows the cumulative number of outliers over one wave period, i.e. cells of extreme strain rate magnitude. Fig. 12 (c) shows the temporally- and domain-averaged strain rate outliers found at the interface for all five wave forcings with $\nu \approx 0.01$ m$^2$ s$^{-1}$, $\nu \approx 0.04$ m$^2$ s$^{-1}$, and $\nu \approx 0.16$ m$^2$ s$^{-1}$. The number of interface FVM cells gives an indication for strain rate localisation due to form drag, and shows a similar trend as previously found for the ice floe collision pattern. The smaller wave periods, $T < 16$ s, show a higher number of interface FVM cells, whereas the number of interface FVM cells is smaller for the larger wave periods, $T \geq 16$ s. The mean strain rate at the interface, however, increases for increasing wave period. From this inverse relationship it can be concluded that larger wave periods lead to

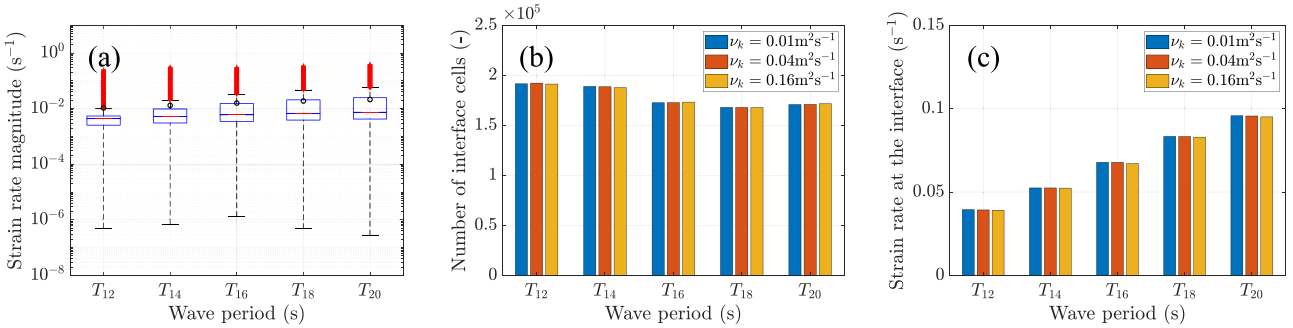


**Fig. 12.** **(a)** Box plots with the strain rate magnitude of all grease ice FVM cells in the inner domain over one wave period with $\nu \approx 0.04$ m$^2$ s$^{-1}$ for wave periods $T = 12 - 20$ s, **(b)** number of strain rate outliers accumulated over one wavelength for kinematic grease ice viscosity values ranging from $\nu \approx 0.01 - 0.16$ m$^2$ s$^{-1}$, and **(c)** temporally- and domain-averaged strain rate outliers at the interface over one wave period for $\nu \approx 0.01 - 0.16$ m$^2$ s$^{-1}$.

stronger strain rate localisation due to form drag.

As previously found for the collision stress of ice floes, variations in viscosity do not significantly affect the number of outliers and mean strain rate values at the interface. This is mainly due to the relatively small range of viscosity values away from the singularity values, and because the small-scale model imposes the wave properties. As for the floe dynamics, a dissipating wave would result in a reduction of the strain rates but the wave energy loss in a small spatial domain can be disregarded.

Lastly, Fig. 13 shows the spatially averaged strain rate values at the interface (values > maximum whisker length, Fig. 13(a)) and in between ice floes, away from the interface (values < maximum whisker length, Fig. 13(b)), for wave forcing with $T = 12$ s, $T = 16$ s and $T = 20$ s. Both, the strain rate magnitude at the ice floe interface and away from the interface show a direct correlation with increasing wave period. Moreover, the values at the interface are approximately one order of magnitude greater than the grease ice strain rate magnitudes in between ice floes.

## 4. Conclusions

A numerical analysis of the dynamics of sea ice in the Antarctic marginal ice zone on the sub-kilometre scale has been conducted. The small-scale model, developed in the computational fluid dynamics (CFD) software OpenFOAM, makes use of a continuum approach separately modelling solid and fluid-like ice cover constituents by suitable materials laws. This approach allows for the detailed study of mechanical interaction between ice floes and interstitial grease ice as well as ice floe collision dynamics.

The relative motion between the sea ice cover and the ocean layer underneath is strongly affected by the sea ice layout and the wave forcing. The wind and ocean current velocities were set to zero assuming that local fluctuations of wind and ocean current velocities are relatively small at the sub-kilometre scale. Accordingly, the orbital wave velocity governs sea ice interaction exhibiting a near negligible sea ice drift. Generally, stress due to the Froude-Krylov force, acting at the circumference of ice floes, results in ice floe stress which is several orders of magnitude greater than stress acting in grease ice. Furthermore, a phase shift can be observed between the sea ice velocity and the wave orbital velocity due to inertia, which increases for increasing wave period, for a prescribed wave steepness. This phase shift leads to a less straightforward interplay between the sea ice velocity, wave elevation and collision stress intensity. For a steepness that corresponds to storm conditions, smaller wave periods, with $T < 16$ s, result in little ice floe collisions, with mainly the same ice floes colliding over time and an oscillating collision stress intensity. A larger number of ice floes collide for longer wave periods, with $T \geq 16$ s, due to a higher kinetic wave energy in the system. Therefore, the number of ice floe collisions and the collision stress intensity gradually increase for increasing wave periods.

The effects of floe inertia and form drag within the surrounding grease ice were demonstrated with respect to velocity and strain rate distributions. Both exhibit high localised gradients at the floe-grease ice interface. The number of interface FVM cells, represented by extreme strain rate magnitude values due to form drag, shows a similar correlation as previously found for the collision pattern. Smaller wave periods, with $T < 16$ s, show a higher number of interface FVM cells, whereas the number of interface FVM cells is smaller for the larger wave periods, with $T \geq 16$ s. Therefore, for smaller wave periods, form drag of solitary floes is more pronounced, i.e. a "thicker" interface between ice floes and grease ice, as indicated by a higher number of extreme strain rate magnitude values. This, however, does not affect the temporally- and domain-averaged strain rate magnitude at the interface, as the results show higher values for increasing wave period.

It was shown that increasing grease ice viscosity within the range of viscosity which reflect in-situ conditions barely affects the sea ice stress and strain rate response. The resulting mechanical response exhibits negligibly small differences. Additionally, an imposed harmonic wave is considered whereas a freely propagating wave in sea ice would dissipate energy, affecting both the stress and strain rate response. However, this effect can be neglected, due to the small size of the considered sea ice domain, over which dissipation in the field for comparable conditions is estimated to be <1% (Alberello et al., 2022).

The used grease ice rheology suffers from a singularity, resulting in locally very high viscosity values, when strain rate values approach zero. As a result, viscosity values not affected by the singularity in the inner domain are underestimated. Consequently, the difference between the three considered kinematic viscosity values is also to some degree underestimated. Additionally, the singularity results in a stress discontinuity in grease ice, which ideally should be more gradual. This is still an aspect in the model which requires further investigation.

The presented approach serves as pioneering work of small-scale sea ice modelling in a continuum framework. It demonstrates its general applicability to describe the collision dynamics of ice floes embedded in grease ice. This work strictly focused on the interaction between the heterogeneous sea ice layer for a range of different wave periods. Note, however, that the sensitivity of sea ice dynamics in the MIZ to other physical parameters can be studied separately in future work, as the approach presented can be used to investigate dependency on particular variables of interest for specific engineering applications. It is believed that the model could also provide new insights concerning atmosphere-ocean physical processes on a scale larger than a kilometre requiring high-resolution modelling. Additionally, the newly-developed model

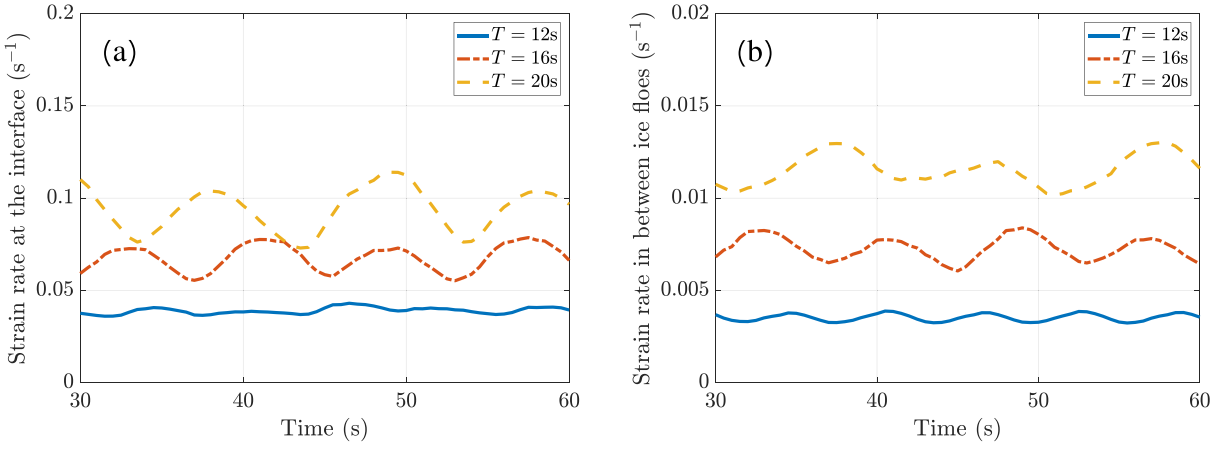


**Fig. 13.** Effect of varying wave forcing on the strain rate response of grease ice, $\dot{\varepsilon}_{mag}$, over time, showing **(a)** at the ice floe-grease ice interface, and **(b)** in between ice floes (away from the interface).

can be used for parametrisation of large-scale models, which contribute to earth system modelling.

## CRediT authorship contribution statement

**Rutger Marquart:** Conceptualization, Methodology, Software, Formal analysis, Writing – original draft, Writing – review & editing, Visualization. **Alfred Bogaers:** Methodology, Software, Formal analysis, Writing – original draft, Writing – review & editing, Supervision. **Sebastian Skatulla:** Conceptualization, Methodology, Formal analysis, Writing – original draft, Writing – review & editing, Supervision, Funding acquisition. **Alberto Alberello:** Writing – original draft, Writing – review & editing, Supervision. **Alessandro Toffoli:** Writing – original draft, Writing – review & editing. **Carina Schwarz:** Writing – original draft, Writing – review & editing.

## Declaration of Competing Interest

The authors have no known competing financial interests or personal relationships that could have appeared to influence the work reported in this paper.

## Data availability

Data will be made available on request.

## Acknowledgements

Computations were performed using facilities provided by the University of Cape Town's ICTS High Performance Computing team: hpc.uct.ac.za. This research has been supported by the National Research Foundation of South Africa (Grant Nos. 104839 and 105858). Opinions expressed and conclusions arrived at, are those of the author and are not necessarily to be attributed to the NRF. AA and AT acknowledge support from the ACE Foundation–Ferring Pharmaceuticals and the Australian Antarctic Science Program (project 4434). AA acknowledges support from the Japanese Society for the Promotion of Science (PE19055).

## References

Alberello, A., Părău, E.I., 2022. A dissipative nonlinear schrödinger model for wave propagation in the marginal ice zone. Phys. Fluids 34, 061702. https://doi.org/10.1063/5.0089866.

Alberello, A., Onorato, M., Bennetts, L., Vichi, M., Eayrs, C., MacHutchon, K., Toffoli, A., 2019. Brief communication: Pancake ice floe size distribution during the winter expansion of the antarctic marginal ice zone. Cryosphere 13, 41–48.

Alberello, A., Bennetts, L., Heil, P., Eayrs, C., Vichi, M., MacHutchon, K., Onorato, M., Toffoli, A., 2020. Drift of pancake ice floes in the winter antarctic marginal ice zone during polar cyclones. J. Geophys. Res. Oceans 125 e2019JC015418.

Alberello, A., Bennetts, L.G., Onorato, M., Vichi, M., MacHutchon, K., Eayrs, C., Ntamba, B.N., Benetazzo, A., Bergamasco, F., Nelli, F., et al., 2022. Three-dimensional imaging of waves and floes in the marginal ice zone during a cyclone. Nat. Commun. 13, 1–11.

Andreas, E.L., Tucker III, W.B., Ackley, S.F., 1984. Atmospheric boundary-layer modification, drag coefficient, and surface heat flux in the antarctic marginal ice zone. J. Geophys. Res. Oceans 89, 649–661.

Bennetts, L., Williams, T., 2015. Water wave transmission by an array of floating discs. Proc. Royal Soc. A Math. Phys. Eng. Sci. 471, 20140698.

Damsgaard, A., Adcroft, A., Sergienko, O., 2018. Application of discrete element methods to approximate sea ice dynamics. J. Adv. Model. Earth Syst. 10, 2228–2244.

De Santi, F., Olla, P., 2017. Effect of small floating disks on the propagation of gravity waves. Fluid Dyn. Res. 49, 025512.

De Santi, F., De Carolis, G., Olla, P., Doble, M., Cheng, S., Shen, H.H., Wadhams, P., Thomson, J., 2018. On the ocean wave attenuation rate in grease-pancake ice, a comparison of viscous layer propagation models with field data. J. Geophys. Res. Oceans 123, 5933–5948.

Derkani, M.H., Alberello, A., Nelli, F., Bennetts, L.G., Hessner, K.G., MacHutchon, K., Reichert, K., Aouf, L., Khan, S., Toffoli, A., 2021. Wind, waves, and surface currents in the southern ocean: observations from the antarctic circumnavigation expedition. Earth Syst. Sci. Data 13, 1189–1209. https://doi.org/10.5194/essd-13-1189-2021.

Doble, M.J., 2009. Simulating pancake and frazil ice growth in the weddell sea: a process model from freezing to consolidation. J. Geophys. Res. Oceans 114.

Doble, M.J., Coon, M.D., Wadhams, P., 2003. Pancake ice formation in the weddell sea. J. Geophys. Res. Oceans 108.

Eayrs, C., Holland, D., Francis, D., Wagner, T., Kumar, R., Li, X., 2019. Understanding the seasonal cycle of antarctic sea ice extent in the context of longer-term variability. Rev. Geophys. 57, 1037–1064.

Herman, A., 2016. Discrete-Element bonded-particle Sea Ice model DESIgn, version 1.3a - Model description and implementation. Geosci. Model Dev. 9, 1219–1241. https://doi.org/10.5194/gmd-9-1219-2016.

Herman, A., 2018. Wave-induced surge motion and collisions of sea ice floes: finite-floe-size effects. J. Geophys. Res. Oceans 123, 7472–7494.

Herman, A., Cheng, S., Shen, H.H., 2019. Wave energy attenuation in fields of colliding ice floes–part 2: a laboratory case study. Cryosphere 13, 2901–2914.

Hibler, W.D., 1979a. A dynamic thermodynamic sea ice model. J. Phys. Oceanogr. 9, 815–846. https://doi.org/10.1175/1520-0485(1979)009<0815:ADTSIM>2.0.CO;2.

Hibler, W.D., 1979b. A viscous sea ice law as a stochastic average of plasticity. J. Geophys. Res. C 206–209.

Holthuijsen, L.H., 2007. Waves in Oceanic and Coastal Waters, 1st ed. Cambridge University Press. https://doi.org/10.1017/CBO9780511618536.

Hopkins, M.A., 1996. On the mesoscale interaction of lead ice and floes. J. Geophys. Res. Oceans 101, 18315–18326.

Hunke, E.C., Dukowicz, J.K., 1997. An elastic – viscous – plastic model for sea ice dynamics. J. Phys. Oceanogr. 27, 1849–1867. https://doi.org/10.1175/1520-0485.

Kohout, A.L., Meylan, M.H., Plew, D.R., 2011. Wave attenuation in a marginal ice zone due to the bottom roughness of ice floes. Ann. Glaciol. 52, 118–122.

Kohout, A., Williams, M., Dean, S., Meylan, M., 2014. Storm-induced sea-ice breakup and the implications for ice extent. Nature 509, 604–607.

Kohout, A.L., Smith, M., Roach, L.A., Williams, G., Montiel, F., Williams, M.J., 2020. Observations of exponential wave attenuation in antarctic sea ice during the pipers campaign. Ann. Glaciol. 61, 196–209.

Leppäranta, M., Hibler, W.D., 1985. The role of plastic ice interaction in marginal ice zone dynamics. J. Geophys. Res. 90, 11899. https://doi.org/10.1029/JC090iC06p11899.

Li, H., Gedikli, E.D., Lubbad, R., Nord, T.S., 2020. Laboratory study of wave-induced ice-ice collisions using robust principal component analysis and sensor fusion. Cold Reg. Sci. Technol. 172, 103010.

Lu, P., Li, Z., Cheng, B., Leppäranta, M., 2011. A parameterization of the ice-ocean drag coefficient. J. Geophys. Res. Oceans 116.

Marquart, R., Bogaers, A., Skatulla, S., Alberello, A., Toffoli, A., Schwarz, C., Vichi, M., 2021. A computational fluid dynamics model for the small-scale dynamics of wave, ice floe and interstitial grease ice interaction. Fluids 6, 176.

Massom, R.A., Stammerjohn, S.E., 2010. Antarctic sea ice change and variability - Physical and ecological implications. Polar Sci. 4, 149–186. https://doi.org/10.1016/j.polar.2010.05.001.

McGuinness, M., Williams, M., Langhorne, P., Purdie, C., Crook, J., 2009. Frazil deposition under growing sea ice. J. Geophys. Res. Oceans 114.

Montiel, F., Squire, V., Doble, M., Thomson, J., Wadhams, P., 2018. Attenuation and directional spreading of ocean waves during a storm event in the autumn Beaufort Sea marginal ice zone. J. Geophys. Res. Oceans 123, 5912–5932.

Montiel, F., Kohout, A.L., Roach, L.A., 2022. Physical drivers of ocean wave attenuation in the marginal ice zone. J. Phys. Oceanogr. 52, 889–906.

Newyear, K., Martin, S., 1999. Comparison of laboratory data with a viscous two-layer model of wave propagation in grease ice. J. Geophys. Res. Oceans 104, 7837–7840.

Paul, F., Mielke, T., Schwarz, C., Schröder, J., Rampai, T., Skatulla, S., Audh, R.R., Hepworth, E., Vichi, M., Lupascu, D.C., 2021. Frazil ice in the antarctic marginal ice zone. J. Mar. Sci. Eng. 9, 647.

Rabatel, M., Labbé, S., Weiss, J., 2015. Dynamics of an assembly of rigid ice floes. J. Geophys. Res. Oceans 120, 5887–5909.

Rabault, J., Sutherland, G., Jensen, A., Christensen, K.H., Marchenko, A., 2019. Experiments on wave propagation in grease ice: combined wave gauges and particle image velocimetry measurements. J. Fluid Mech. 864, 876–898.

Radia, N.V., 2014. Frazil Ice Formation in the Polar Oceans. Ph.D. thesis.. UCL (University College London).

Roach, L.A., Smith, M.M., Dean, S.M., 2018. Quantifying growth of pancake sea ice floes using images from drifting buoys. J. Geophys. Res. Oceans 123, 2851–2866.

Roenby, J., Bredmose, H., Jasak, H., 2016. A computational method for sharp interface advection. R. Soc. Open Sci. 3, 160405.

Roenby, J., Bredmose, H., Jasak, H., 2019. Isoadvector: Geometric vof on general meshes. In: OpenFOAM. Springer, pp. 281–296.

Rogers, W.E., Thomson, J., Shen, H.H., Doble, M.J., Wadhams, P., Cheng, S., 2016. Dissipation of wind waves by pancake and frazil ice in the autumn b eaufort s ea. J. Geophys. Res. Oceans 121, 7991–8007.

Schulkes, R., Morland, L., Staroszczyk, R., 1998. A finite-element treatment of sea ice dynamics for different ice rheologies. Int. J. Numer. Anal. Methods Geomech. 22, 153–174.

Shapiro, L.H., Johnson, J.B., Sturm, M., Blaisdell, G.L., 1997. Snow Mechanics: Review of the State of Knowledge and Applications. Technical Report. Cold Regions Research and Engineering Laboratory, Hanover, New Hampshire 03755-1290.

Shen, H.H., Hibler III, W.D., Leppäranta, M., 1987. The role of floe collisions in sea ice rheology. J. Geophys. Res. Oceans 92, 7085–7096.

Skatulla, S., Audh, R.R., Cook, A., Hepworth, E., Johnson, S., Lupascu, D.C., MacHutchon, K., Marquart, R., Mielke, T., Omatuku, E., et al., 2022. Physical and mechanical properties of winter first-year ice in the antarctic marginal ice zone along the good hope line. Cryosphere 16, 2899–2925.

Smith, M., Thomson, J., 2020. Pancake sea ice kinematics and dynamics using shipboard stereo video. Ann. Glaciol. 61, 1–11.

Squire, V.A., 2020. Ocean wave interactions with sea ice: a reappraisal. Annu. Rev. Fluid Mech. 52.

Sutherland, G., Rabault, J., Christensen, K.H., Jensen, A., 2019. A two layer model for wave dissipation in sea ice. Appl. Ocean Res. 88, 111–118.
Thorndike, A.S., Rothrock, D.A., Maykut, G.A., Colony, R., 1975. The thickness distribution of sea ice. J. Geophys. Res. 80, 4501. https://doi.org/10.1029/JC080i033p04501.
Vichi, M., Eayrs, C., Alberello, A., Bekker, A., Bennetts, L., Holland, D., de Jong, E., Joubert, W., MacHutchon, K., Messori, G., Mojica, J.F., Onorato, M., Saunders, C., Skatulla, S., Toffoli, A., 2019. Effects of an explosive polar cyclone crossing the antarctic marginal ice zone. Geophys. Res. Lett. 46, 5948–5958.
Wadhams, P., Parmiggiani, F., de Carolis, G., 2006. Wave dispersion by antarctic pancake ice from sar images: A method for measuring ice thickness. In: Advances in SAR Oceanography from Envisat and ERS Missions, p. 36.
Wang, R., Shen, H.H., 2010. Cold regions science and technology experimental study on surface wave propagating through a grease – pancake ice mixture. Cold Reg. Sci. Technol. 61, 90–96. https://doi.org/10.1016/j.coldregions.2010.01.011.
Worby, A.P., Geiger, C.A., Paget, M.J., Van Woert, M.L., Ackley, S.F., DeLiberty, T.L., 2008. Thickness distribution of Antarctic sea ice. J. Geophys. Res. Oceans 113.
Yiew, L.J., Bennetts, L., Meylan, M., Thomas, G., French, B., 2017. Wave-induced collisions of thin floating disks. Phys. Fluids 29, 127102.
Zhao, X., Shen, H.H., 2015. Cold regions science and technology wave propagation in frazil / pancake, pancake, and fragmented ice covers. Cold Reg. Sci. Technol. 113, 71–80. https://doi.org/10.1016/j.coldregions.2015.02.007.
Zhao, X., Shen, H.H., 2018. Three-layer viscoelastic model with eddy viscosity effect for flexural-gravity wave propagation through ice cover. Ocean Model 131, 15–23.